Separation and Purification Technology 286 (2022) 120467

Contents lists available at ScienceDirect

Separation and Purification Technology

journal homepage: www.elsevier.com/locate/seppur

Solar photocatalytic degradation of parabens using UiO-66-NH_2

Manuel Peñas-Garzón [a,b], Maria J. Sampaio [b,*], Yilan L. Wang [a], Jorge Bedia [a], Juan J. Rodriguez [a], Carolina Belver [a,*], Claudia G. Silva [b], Joaquim L. Faria [b]

[a] Chemical Engineering Department, Universidad Autónoma de Madrid, Campus Cantoblanco, E-28049 Madrid, Spain
[b] Laboratory of Separation and Reaction Engineering – Laboratory of Catalysis and Materials (LSRE-LCM), Faculdade de Engenharia, Universidade do Porto, Rua Dr. Roberto Frias s/n, 4200-465 Porto, Portugal

ARTICLE INFO

Keywords:
Methylparaben
UiO-66-NH_2
Solar photocatalysis
WWTP effluent
Continuous flow mode
Photocatalytic mechanism

ABSTRACT

The photocatalytic degradation of methylparaben was investigated under simulated solar light using a synthesised metal–organic framework (UiO-66-NH_2). For that purpose, the pollutant was spiked in different water matrices: distilled water, water from Lima River (Northwestern Portugal), and urban wastewater. Complete removal of the methylparaben in distilled water was achieved in 1 h reaction. In natural water matrices, the photocatalytic performance decreased to 70% removal after 3 h reaction, owing to the physical–chemical properties of the water samples. The UiO-66-NH_2 photocatalyst revealed high stability under the continuous mode, reaching a steady state in 5 h, from which the removal percentage was kept constant for 25 h. The photocatalytic degradation of methylparaben gave five main reaction byproducts and four short-chain carboxylic acids, identified by LC/ESI-MS and UHPLC analyses, respectively. The mechanism of degradation was investigated by using selective scavengers. Photogenerated holes and superoxide radicals were found as the main species responsible for the degradation of methylparaben. The abatement of other parabens (as ethyl- and propylparaben) was also evaluated, being the conversion influenced by the length of the alkyl side chain. The results of this study give a comprehensive sight into the effective photocatalytic remediation of parabens using UiO-66-NH_2.

1. Introduction

Parabens (alkyl side chains based *p*-hydroxybenzoates) are extensively used as preservatives and antimicrobial/antifungal agents in the formulation of cosmetics, pharmaceuticals and food commodities [1] owing to their capacity to disrupt cell membranes and intracellular proteins while conditioning enzymatic activity [2]. Its use in personal care products is considered to be non-toxic to humans at the maximum concentration allowed in those commercial products (0.4% w/w) [3], although it is associated with an increased risk of atopic dermatitis reactions [4]. These compounds can be introduced into the water cycle by using pharmaceuticals and personal care products (PPCPs), as proved by their detection in human tissues and urine samples [5]. Their presence in natural water bodies and specifically in wastewaters (up to 120 $\mu g \cdot L^{-1}$ for methylparaben, the most identified paraben in wastewater treatment plants (WWTPs) inlet streams [6]) as a consequence of the not complete elimination in WWTPs (ranging from 25.9% to total removal) [7] can affect the reuse of treated wastewater negatively. Besides, the endocrine disruptor character of parabens derived into their classification as contaminants of emerging concern by the U.S. Environmental Protection Agency [8], establishing certain limitations for their use in cosmetic and food industries in Europe [3].

Among the parabens family, the compounds more frequently detected are methyl-, ethyl- and propylparaben (MP, EP and PP, respectively). Several technological approaches for the abatement of these compounds have been reported, including adsorption [9], activated sludge [10] and advanced oxidation processes (AOPs) as ozonation [11] or heterogeneous photocatalysis [12]. Regarding the photocatalytic removal of parabens, TiO_2 has been widely investigated [13,14]. However, its photocatalytic efficiency is reduced under solar irradiation owing to the wide bandgap ($E_g \approx 3.2$ eV) that partially hinders the light-harvesting from the visible region. Modifications of this photocatalyst, as well as the design and preparation of different ones, have been explored to improve the solar light-driven photocatalytic elimination of parabens [15]. The photocatalytic removal of MP has been reported with TiO_2 P25 [12,16], with different photocatalysts based on g-C_3N_4 [17] or $Bi_4O_5Br_2$

* Corresponding authors.
E-mail addresses: mjsampaio@fe.up.pt (M.J. Sampaio), carolina.belver@uam.es (C. Belver).

https://doi.org/10.1016/j.seppur.2022.120467
Received 14 October 2021; Received in revised form 28 December 2021; Accepted 6 January 2022
Available online 10 January 2022

[18] under different radiations (as summarised in Table S1).

As part of the new photocatalytic materials for environmental applications, the development of metal–organic frameworks (MOFs) has gained increasing interest. MOFs are crystalline porous materials constituted by clusters of metal ion nodes (mainly Fe-, Ti- or Zr-based ones) connected through organic linkers [19,20]. These materials are characterised by a well-developed porous texture and outstanding optical properties as semiconductors [21], therefore allowing their use for several purposes as gas storage or photocatalytic water treatment [22]. Regarding this last application, some works report the removal of PPCPs using MOFs, highlighting the elimination of the pharmaceuticals acetaminophen [23], diclofenac [24], tetracycline [25] or ciprofloxacin [26], among others. Recently, the photocatalytic degradation of organic pollutants has been investigated using Zr-based MOFs (as UiO-66 series) due to their remarkable activity and their stability in aqueous media [27–29]. For example, the solar-driven conversion of acetaminophen was evaluated using UiO-66 based MOFs [30]. The presence of an amine group in the ligand, leading to UiO-66-NH_2, resulted in a higher light-harvesting from the visible region and better photocatalytic performance than the unmodified MOF. This MOF, forming a composite with ZnO, also proved the good photocatalytic activity in the degradation of tetracycline [31]. The successful synthesis of heterojunctions using other Zr-based MOF, UiO-67, and their use for the photocatalytic removal of the antibiotic ofloxacin [32] has also been reported, with the complete conversion after 3 h under solar light.

To the best of our knowledge, the photocatalytic removal of parabens in aqueous solutions using UiO-66-NH_2 was not previously reported. In this study, preparation, characterization and photocatalytic performance of this MOF are comprehensively described in connection with the neutralization of the threat derived from the presence of parabens in water. Due to the lack of previous information, this work assesses a detailed set of experiments using MP as target paraben regarding the optimal reaction conditions (in terms of photocatalyst dose and pH of the solution) and the use of different water matrices (namely river water and wastewater). The tentative radical mechanism and the degradation pathway are also proposed. In addition, a comparison of the photocatalytic conversion of different parabens is considered (i.e., MP, EP and PP) in both individual and mixture tests. Moreover, MOF stability through successive batch cycles and continuous flow operation is evaluated, giving a complete perspective for the feasible use of UiO-66-NH_2 to abate this type of contaminants under solar light.

2. Materials and methods

2.1. Chemicals and reagents

Zirconium butoxide ($Zr(OC_4H_9)_4$, 80% in 1-butanol), 2-aminoterephthalic acid (ATA, 99%), formic acid (≥95%), HCl (≥37%), 1,4-benzoquinone (p-BQ, ≥98%), KI (≥99%), 2,2,6,6-tetramethyl-1-piperidinyloxy (TEMPO, 99%), 5,5-dimethyl-1-pyrroline N-oxide (DMPO, ≥98%) and the tested parabens, namely methylparaben (MP, $(C_6H_4(OH)COO)CH_3$, 99%), ethylparaben (EP, $(C_6H_4(OH)COO)C_2H_5$, 99%) and propylparaben (PP, $(C_6H_4(OH)COO)C_3H_7$, ≥99%) were all purchased from Sigma-Aldrich. Table S2 collects the main physicochemical properties of these parabens. Acetonitrile (ACN, HPLC grade), NaOH (≥95%) and Na_2SO_4 (≥99%) were supplied by Scharlab. N,N-dimethylformamide (DMF, 99.8%), H_3PO_4 (85%) and 2-propanol (99.7%) were purchased from PanReac AppliChem. Methanol (MeOH, ≥99.8%) and $AgNO_3$ (≥99%) were supplied by Honeywell and Alfa Aesar, respectively. Unless otherwise indicated, distilled water (Type II) was used throughout the work.

2.2. Synthesis of UiO-66-NH_2 MOF

UiO-66-NH_2 was prepared following a synthesis procedure previously reported [33], being modified by using ($Zr(OC_4H_9)_4$) and ATA as the metal precursor and organic linker, respectively. As schematised in Fig. 1, $Zr(OC_4H_9)_4$ (1.5 mmol) and ATA (1.5 mmol) were placed in a 100 mL Schott bottle and dissolved in DMF (20 mL). Then, the solution was ultrasonicated for 8 min to obtain a transparent yellow solution. Formic acid (10 mL) was dropwise added to the mixture, and it was furtherly ultrasonicated for 2 min. The bottle was sealed using an airtight Schott bottle cap, and the solution was heated at 120 °C for 24 h in a Memmert UN30 oven. After cooling to room temperature, the solid was recovered by centrifugation (9000 rpm, 2 min), and washed three times with fresh DMF (first time: 1 h; following ones: 20 min) and subsequently, three times with MeOH (first time: 24 h; successive ones: 20 min) as a solvent exchanger. The resulting material was centrifuged and dried under vacuum at 70 °C for 12 h and finally stored.

2.3. Characterisation of photocatalyst

A Bruker D8 diffractometer (Cu-Kα source, λ = 0.15406 nm; 2θ = 5-50°) was used to determine the X-ray diffraction (XRD) pattern. The morphology of the material was observed by scanning electron microscopy (SEM) using a Quanta 3D Field Emission Gun (FEG) microscope (FEI Company). A Micromeritics TriStar 123 static volumetric apparatus was used to assess the porous texture by N_2 adsorption–desorption at −196 °C. The material was previously degassed under vacuum at 120 °C for 16 h. The Brunauer-Emmett-Teller (BET) method [34] was used to determine the specific surface area (S_{BET}), while the *t*-plot method [35] was used for the microporous area and micropore volume (S_{MP} and V_{MP}, respectively). Total pore volume (V_T) was obtained by the amount of adsorbed nitrogen at a relative pressure (P/P_0) of 0.99. The UV–vis diffuse reflectance (UV–vis DRS) spectrum was determined using a Shimadzu 2600 UV–vis spectrophotometer, using $BaSO_4$ as the reference material. The bandgap (E_g) value was estimated by the Tauc plot method [36] considering UiO-66-NH_2 as an indirect semiconductor [30]. The pH at the point of zero charge (pH_{PZC}) was determined using the drift method [37]. X-ray photoelectron spectroscopy (XPS) spectra were recorded using a PHI VersaProbe II spectrometer and Al Kα X-ray (1486.68 eV) as the excitation source. C 1 s peak at 284.5 eV was used as the internal reference. Mott-Schottky plot was obtained applying a voltage between −1.5 and 0.4 V under different scan frequencies (10, 100 and 500 Hz) using a Metrohm Autolab PGSTAT204 station. The material suspension (1 $mg{\cdot}mL^{-1}$) was prepared in 0.1 M Na_2SO_4 (pH ~ 4.1 at 25 °C) and placed into the electrochemical cell (DropSens ITO10). This cell configuration comprises an indium tin oxide (ITO) working electrode, with counter and reference counterparts of carbon and silver electrodes, respectively. The flat band potential of the material, V_{FB}, was obtained following Mott–Schottky equation (Eq. (1)) [38]:

$$\frac{1}{C^2} = \frac{2}{\varepsilon{\cdot}\varepsilon_0{\cdot}e{\cdot}N_D}{\cdot}\left(V - V_{FB} - \frac{k{\cdot}T}{e}\right) \quad (1)$$

being C the capacitance of the semiconductor-electrolyte junction at applied voltage V; ε and ε_0 the permittivity of the semiconductor and the void, respectively; e the electron charge; k the Boltzmann's constant; and T the temperature. The plot of $1/C^2$ *vs* V allows us to estimate the V_{FB} from the intercept point of the tangent line with the potential axis. The conduction band potential (V_{CB}) can be calculated with respect to the normal hydrogen electrode (NHE) at pH 7 following a Nernstian shift using Eq. (2) [39]:

$$V_{CB} = V_{FB(Ag/AgCl,\ pH)} + \Delta V_{(Ag/AgCl,\ NHE)} - 0.059{\cdot}(7 - pH) \quad (2)$$

where $\Delta V_{(Ag/AgCl,\ NHE)}$ is the Ag/AgCl potential against NHE (0.21 V). Finally, the valence band potential (V_{VB}) can be estimated following Eq. (3):

$$V_{VB} = V_{CB} + E_g/e \quad (3)$$

where E_g is the bandgap of the semiconductor. A Bruker EMX (X band) spectrometer (with an ER4123D dielectric resonator using a capillary

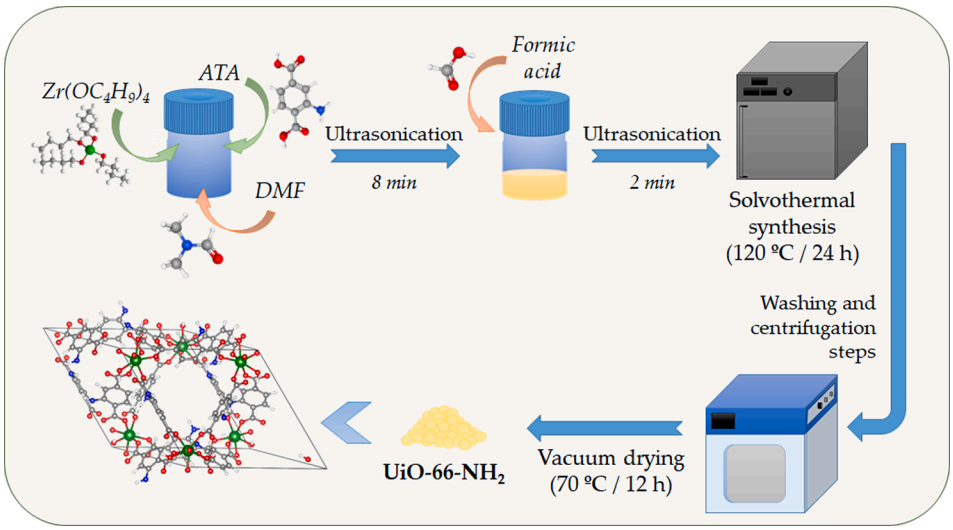

Fig. 1. Schematic diagram for the preparation of UiO-66-NH_2.

quartz tube) was used to carry out the ESR spin-trap experiments. UV irradiation in situ ESR measurements was performed using a high-pressure mercury lamp (Bruker, UV Irradiation System, ER 203 UV), the capillary tube inside the cavity being irradiated at different times. The instrumental settings were as follows: centre field = 3480 G; sweep width = 300 G; microwave power = 0.2 mW; modulation amplitude = 1.0 G; modulation frequency = 100 kHz; receiver gain = $1.261 \cdot 10^4$; time constant = 81.92 ms; sweep time = 20.97 s; resolution in × = 1024 points; number of scans = 1. The capillary tube was filled with 10 µL of a water/TEMPO solution (2 mM) containing the catalyst suspended in a ratio of 0.25 µg·µL^{-1}. Similar experiments were carried out with 5,5-dimethyl-1-pyrroline N-oxide (DMPO), using a solution water/DMPO (50 mM) or methanol/DMPO (50 mM) for the detection of $HO^{\bullet}$ and $O_2^{\bullet-}$ radicals, respectively.

2.4. Photocatalytic performance

Unless otherwise indicated, the photocatalytic experiments were performed in distilled water for 3 h under simulated solar light using a Solarbox 1500e (CO.FO.ME.GRA). The apparatus was equipped with a 1500 W Xenon lamp (600 W·m^{-2}), a cut-off soda-lime glass UV filter (restrains λ less than 290 nm) and an infrared reflection coating to simulate the outdoor exposure. In a typical batch experiment, a photocatalyst dose of 0.75 g·L^{-1} was dispersed in 50 mL of MP solution (32.9 µM, corresponding to 5 mg·L^{-1}) placed in a borosilicate glass cylindrical reactor (300 mL, 8.0 cm of internal diameter) covered with transparent film. Before illumination, the photocatalyst and the paraben solution were left in the dark for 1 h to establish the adsorption–desorption equilibrium. The experiments were performed under continuous magnetic stirring, being the solution saturated with air (~50 mL·min^{-1}) and at natural pH (5.5). The temperature during the photocatalytic experiment was set at 30 ± 2 °C. Preliminary photocatalytic tests for the removal of MP were performed in terms of photocatalyst dose (0.25–1.00 g·L^{-1}) and solution pH (4.5–9.5). In those experiments, the pH of the solution was modified using 0.1 M HCl or NaOH solutions. The apparent pseudo-first-order rate constant of MP disappearance (k_{app}, min^{-1}) was obtained by fitting Eq. (4):

$$\ln\left(\frac{[MP]_t}{[MP]_{t=0}}\right) = -k_{app} \cdot t \Leftrightarrow \ln(1 - X_{MP}) = k_{app} \cdot t \quad (4)$$

where $[MP]_t$ and $[MP]_{t=0}$ are the concentrations of MP at reaction time t and 0 (just before turning on the irradiation source), respectively, and X_{MP} is the MP photocatalytic conversion.

Once determined the optimal reaction parameters, the photocatalytic performance was investigated in different water matrices. Specifically, surface water samples were collected from the Lima River in Northwestern Portugal and secondary-treated wastewater from an urban wastewater treatment plant (UWWTP) in Northern Portugal. The removal of other paraben compounds, like EP and PP, was investigated individually and in the mixture of the three parabens (MP, EP and PP). Since the adsorption capacity of the MOF for each compound was different (not shown), the initial concentration of EP and PP was adjusted before the photocatalytic reactions (light on), ensuring similar experimental conditions. Scavenger experiments (1 mM, added before the illumination) were performed using 2-propanol as $HO^{\bullet}$ quencher, KI to trap h^+, as well as $AgNO_3$ and p-BQ to quench e^- and $O_2^{\bullet-}$ [40], respectively. The removal of MP (32.9 µM) spiked in distilled water using a continuous flow system (Figure S1) under solar light was also investigated. A slurry configuration under continuous stirring was followed, keeping constant the solution volume (250 mL) using two peristaltic pumps (0.8 mL·min^{-1}) at the entry and exit of the reactor. The solution was saturated with air, and a filter at the sample intake was set at 0.5 cm under the liquid surface to avoid the loss of the photocatalyst within the outlet flow, thus keeping constant the concentration of photocatalyst inside the reactor. All experiments were assessed in duplicate and average values were included. A third experiment was performed in case of more than 5% difference of the duplicates.

2.5. Analytical techniques

At different time intervals, aliquots (0.4 mL) from the reaction medium were taken and centrifuged (10 min, 14500 rpm), being the supernatant used for the determination of the contaminant concentration by Ultra-High-Pressure Liquid Chromatography (UHPLC). UHPLC was performed using a Shimadzu Nexera X2 LC-30AD apparatus with an SPD-M20A diode array detector, equipped with a Kinetex XB-C18 100 Å column (100 × 2.1 mm; 1.7 µm particle diameter). An isocratic method of 75/25 %v ACN/H_2O (ultrapure water, Type I) was used as mobile phase, being the flow rate 0.15 mL·min^{-1} at 35 °C. The excitation wavelength for MP, EP and PP was 255 nm in all cases. A Supelcogel C-610H column (300 × 7.8 mm) was used to quantify short-chain carboxylic acids (identified using corresponding standards solutions) at the excitation wavelength of 210 nm. An isocratic 0.1% H_3PO_4 mobile phase was used at a flow rate of 0.5 mL·min^{-1} at 30 °C. The water matrices (Table S3) were characterized following standard methods [41]. A WTW InoLab pHmeter was used for the determination of the pH values. The detection and quantification of nitrates, nitrites, sulfates, phosphates,

and cations were performed by ionic chromatography using a Metrohm 881 Cromaped IC Pro apparatus. The chemical oxygen demand (COD) was determined by colourimetry. A Shimadzu TOC-5000A was used to determine the total organic carbon (TOC). The identification of the MP degradation byproducts by liquid chromatography and electrospray ionisation-mass spectrometry (LC/ESI-MS) was performed using a Bruker Maxis II equipment with electrospray ionisation (ESI positive) under the following conditions: *m/z* range from 50 to 3000, capillary voltage of 3500 V, endplate offset of 500 V and dry heater at 300 °C with a gas flow of 8.0 L·min^{-1}.

3. Results and discussion

3.1. Characterisation of the synthesised UiO-66-NH_2

The diagrams in Fig. 2 depict the analysis of the XPS spectra of UiO-66-NH_2. The full spectrum (Fig. 2a) confirmed the presence of Zr, C, N and O in the synthesised sample. Besides, the surface chemical composition in terms of molar ratio of O/Zr and C/Zr (5.2 and 8.1, respectively) agreed with the stoichiometric value (i.e., 5 and 8, respectively) corresponding to the unitary cell $Zr_{24}O_{120}C_{192}H_{96}N_{24}$. The experimental ratio of N/Zr was slightly lower than the stoichiometric one (0.6 and 1,

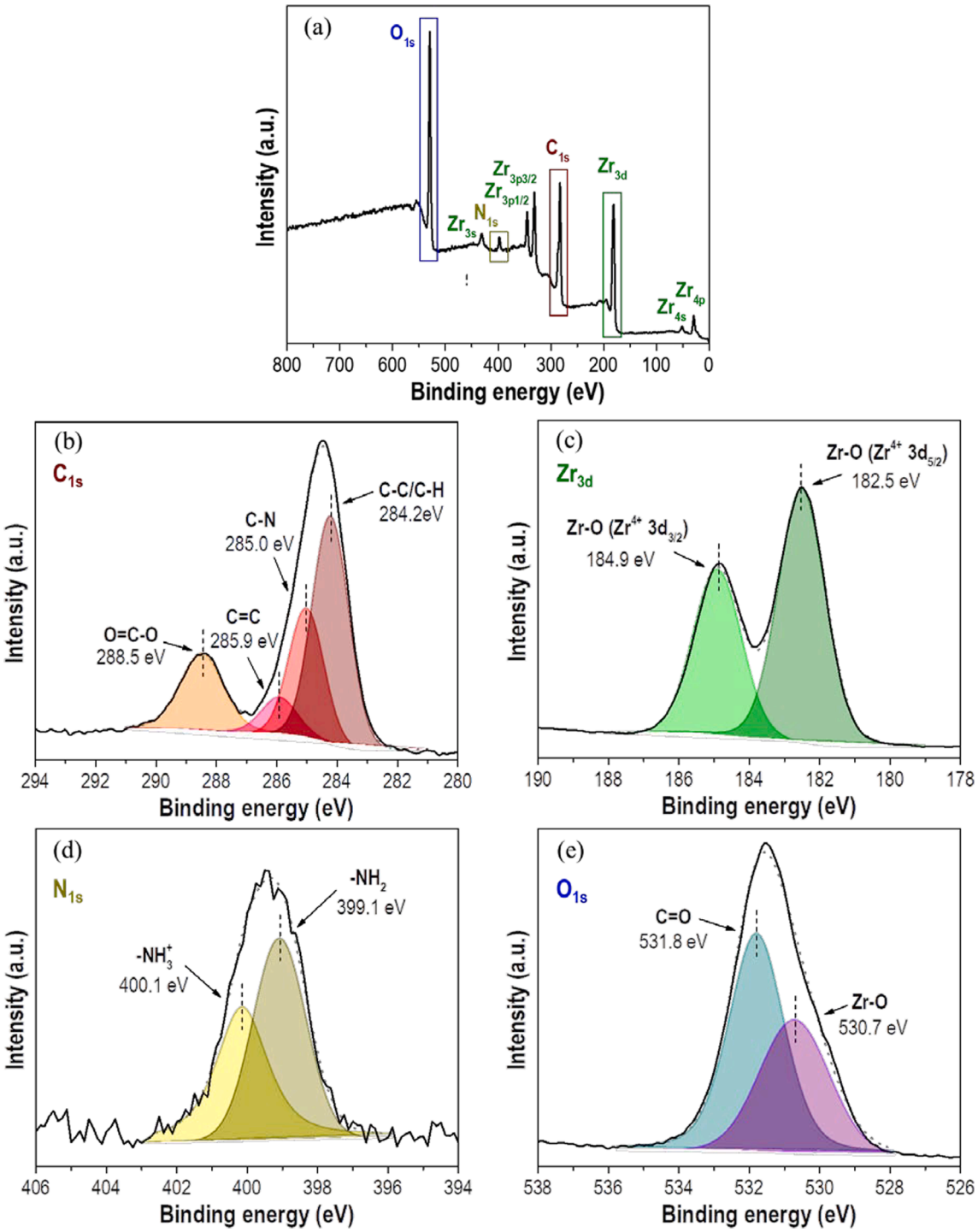

Fig. 2. XPS spectra of UiO-66-NH_2: (a) full spectrum, and high-resolution of (b) C 1 s, (c) Zr 3d, (d) N 1 s and (e) O 1 s.

respectively). The high-resolution spectrum of C 1 s (Fig. 2b) displays the contributions of the carbon species associated with the linker units. The deconvolution revealed the prominent presence of aliphatic sp^3 C-C and C-H (284.2 eV), C-N (285.0 eV), aromatic sp^2 C = C (285.9 eV) and O = C-O (288.5 eV) bonds as previously described [24,42]. Regarding the Zr 3d spectrum (Fig. 2c), two peaks at 182.5 and 184.9 eV were ascribed to Zr^{4+} $3d_{5/2}$ and $3d_{3/2}$ [43,44], respectively, suggesting the suitable formation of Zr-O bonds in the metal cluster. Fig. 2d depicts the N 1 s spectrum, showing the peaks related to the contribution of $–NH_2$ bonded to the phenyl ring of the linker ($–NH_2$, 399.1 eV) and the protonated amidogen form ($–NH_3^+$, 400.1 eV) [45,46]. The deconvolution of the O 1 s spectrum (Fig. 2e) shows the contribution of C = O (531.8 eV) and Zr-O (530.7 eV) species [47].

SEM micrograph of the synthesised UiO-66-NH_2 (Fig. 3a) shows particles of globular aspect with some appearance of triangular prism shape. The morphology of these particles differed from the octahedral one commonly reported in other works related to this MOF [47–49], while the average particle size (125 nm) is similar to that observed in those previous works (150–200 nm). XRD confirmed the crystallisation of UiO-66-NH_2. The pattern shown in Fig. 3b coincides with the previously reported one [50] and with that obtained by the simulation of the crystalline structure using VESTA® software (included in Fig. 3b). The crystallite size was calculated from the most intense peak at $2\theta = 7.33°$ using Scherrer's equation. It was found to be 65.9 nm, more than four times higher than that reported by Tambat et al. [51], suggesting a highly defined crystallinity of the material.

The synthesised MOF depicted a type I isotherm (corresponding to the IUPAC classification) (Fig. 3c), typical of solids with predominant microporous texture. The slope of the horizontal-like branch, and the small hysteresis loop reveal some minor contributions of mesoporosity. The BET surface area (Table 1) was within the range commonly reported for UiO-66-NH_2 (around 800–1100 $m^2 \cdot g^{-1}$) [33,48,52]. The microporous surface area and the micropore volume values (corresponding to more than two-thirds of the total pore volume) support the essentially microporous character of this material. The DFT pore size distribution (inset of Fig. 3c) confirms the narrow microporous network of UiO-66-NH_2, showing a bimodal pore size distribution centred around 1.0 and 1.5 nm. The pH_{pzc} of the sample (3.9, Table 1 and Figure S2) suggested a predominantly acidic surface of the synthesised MOF. Fig. 3d depicts the UV–Vis absorption spectrum of UiO-66-NH_2 displaying two characteristic absorption bands, the first one (≈ 255 nm) usually attributed to the electronic transferences from O to Zr centres in the $[Zr_6O_4(OH)_4]$ metal cluster and the second (≈ 325 nm) related to the transitions of conjugated π electrons from the NH_2-based chromophores of the linker to the $[Zr_6O_4(OH)_4]$ cluster [53].

The bandgap value of the MOF (E_g = 2.85 eV, Table 1), obtained from the Tauc plot (inset of Fig. 3d), was similar or even slightly lower than those reported by Zhang et al. [54] and Ren et al. [47] (i.e., 2.86 and 2.91 eV, respectively). From an optoelectronic point-of-view, this value leaves enough room for the synthesised MOF to harvest irradiation up to 435 nm in the blueish side of visible light of the electromagnetic spectrum.

Table 1
Porous texture characterisation, bandgap value and pH_{PZC} of synthesised UiO-66-NH_2.

S_{BET} ($m^2 \cdot g^{-1}$)	S_{MP} ($m^2 \cdot g^{-1}$)	V_T ($cm^3 \cdot g^{-1}$)	V_{MP} ($cm^3 \cdot g^{-1}$)	E_g (eV)	pH_{PZC}
863	706	0.524	0.338	2.85	3.9

S_{BET}, specific surface area; S_{MP}, micropore surface area; V_T, total pore volume; V_{MP}, micropore volume; E_g, bandgap; and pH_{PZC}, pH at point of zero charge.

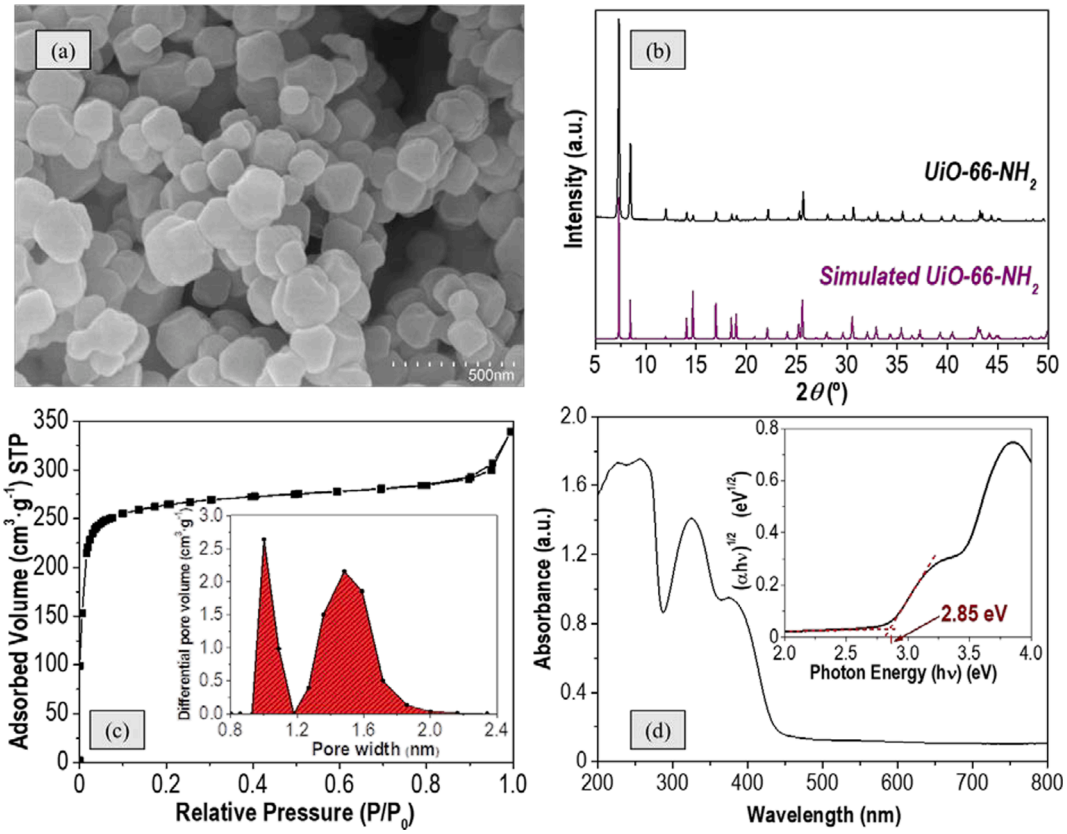

Fig. 3. (a) SEM image, (b) XRD pattern (including the simulated pattern of UiO-66-NH_2 obtained by VESTA® software), (c) N_2 adsorption–desorption isotherm (-196 °C) (Inset: DFT pore size distribution) and (d) UV–vis-DRS spectrum (Inset: Tauc plot) of the synthesised UiO-66-NH_2.

3.2. Photocatalytic tests

3.2.1. Preliminary tests of methylparaben (MP) removal

The photocatalytic performance of the synthesised UiO-66-NH_2 was evaluated in removing MP under simulated solar light at natural pH (pH = 5.5). Before the photocatalytic experiments, the adsorption of the contaminant on the MOF was studied under dark conditions (Figure S3), achieving the adsorption equilibrium in less than 60 min and showing an adsorption capacity of 6.4 μmol·g^{-1}. Preliminary tests were addressed to study the effect of the photocatalyst dose and the pH of the solution (Figs. 4 and S4, respectively). In the absence of photocatalyst (Fig. 4), a slight disappearance (i.e., around 10%) of MP by photolysis was registered after 3 h under solar light. Upon irradiation, the MP conversion increased as the photocatalyst dose increased to a maximum at 0.75 g·L^{-1}, and then conversion decreased probably because the photocatalyst shields the radiation. Figure S4 shows the evolution of the contaminant concentration at different initial pH using 0.75 g·L^{-1} of UiO-66-NH_2. It can be observed that the photocatalytic performance slightly differed within a wide pH range (from 4.0 to 8.5). However, at strong basic conditions (pH = 10), the MP conversion slightly decreased, probably due to the electrostatic repulsions between the negative surface of the photocatalyst (pH_{pzc} = 3.9, Table 1) and the dissociated form of MP (pK_a = 8.17, Table S2). According to the above results, the following experiments were carried out with a photocatalyst dose of 0.75 g·L^{-1} and natural pH (5.5) of the solution.

The literature reports different photocatalysts used to remove MP under solar and visible radiations, as summarized in Table S1. In this respect, it must be highlighted that the use of MOFs for the abatement of MP is herein described for the first time. The different reaction conditions used in the reported studies hinder a suitable comparison among the different materials tested, although the synthesised UiO-66-NH_2 depicts a remarkable photocatalytic performance in terms of MP elimination and apparent pseudo-first-order disappearance rate constant (k_{app} = 7.49·10^{-2} min^{-1}).

3.2.2. Effect of the aqueous matrix

The removal of MP was also assessed in two real aqueous matrices, namely river water and UWWTP secondary-treated effluent. Several studies have reported that organic and inorganic species influence photocatalytic performance during the degradation of contaminants [55,56]. Considering that the complex aqueous framework may have some effect, the main physicochemical characteristics of the water samples were analysed and collected in Table S3. Regarding the inorganic species, as expected, the river and UWWTP samples depicted higher concentrations than the distilled counterparts of Cl^- and SO_4^{2-} anions as well as Na^+, NH_4^+, K^+, Ca^{2+} and Mg^{2+}, and, consequently, higher conductivity. A significant concentration of organic matter was also detected in the UWWTP effluent sample (13.31 mg·L^{-1}). Fig. 5 shows the MP conversion in those water matrices upon photocatalytic treatment with UiO-66-NH_2 under solar irradiation. The resemblance between the experiments made with distilled and river water is noteworthy, reaching almost complete conversion of MP after 1 h, while the UWWTP required 3 h to achieve 70% conversion. This lower photocatalytic performance can be attributed to multiple factors, including light attenuation caused by turbidity (Table S3) and blockage of the photocatalytic surface due to the adsorption of organic matter, among others [17,57].

Moreover, the inorganic ions in UWWTP effluent can act as scavengers of the photogenerated charges (e.g., Cl^- can interact with oxidant species as h^+, allowing the formation of $Cl^•$ or $HClO^{•-}$ and impairing the process [11,55]). To prove this, Figure S5 depicts the conversion of MP in distilled water spiked with Cl^- and SO_4^{2-} at the highest concentration found in the WWTP effluent (Table S3). It can be observed that SO_4^{2-} caused a more pronounced inhibition of MP removal than Cl^-. This inhibition has been attributed by Rioja et al. [58] to the stronger scavenging character of sulphate anions. It can also be inferred from Figure S5 that other factors, as above indicated, reduced the photocatalytic activity in WWTP effluent.

3.2.3. Continuous flow performance and photocatalyst stability

The stability of the photocatalytic performance of synthesised UiO-66-NH_2 was investigated using a continuous flow system. Fresh MP solution ($[MP]_0$ = 32.9 μM) was continuously fed (0.8 mL·min^{-1}) to the solar photocatalytic slurry reactor for 30 h, being around the first 5 h to reach the MP conversion steady state. The catalyst concentration was maintained at 0.75 g·L^{-1}; thus the space–time being 0.12 g_{cat}·h·$μmol_{MP}^{-1}$. Fig. 6 depicts the conversion once the steady state was reached, being observed that the photocatalytic performance was maintained almost constant during the whole experiment (25 h on stream). In the current study, the morphology, crystalline structure and porous texture of the solid obtained after use were characterised (Figure S6), depicting no significant changes compared to the as-prepared catalyst. The results obtained in continuous mode proved a good stability of the MOF in terms of both photocatalytic performances for MP removal and structural resistance.

The performance of NH_2-UiO-66 was further evaluated under four

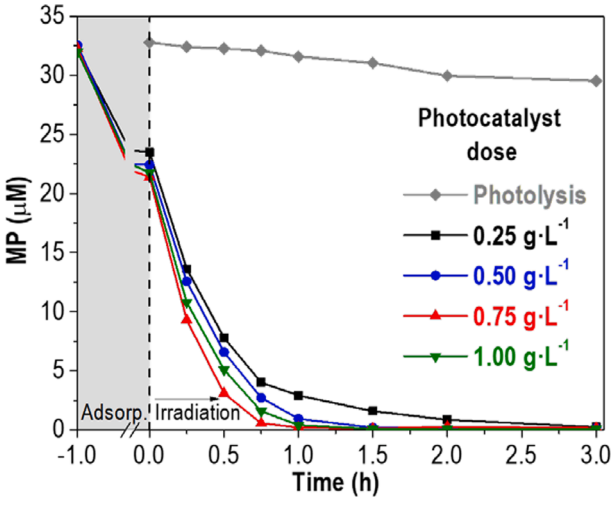

Fig. 4. Time-course of MP concentration using different doses of UiO-66-NH_2 under solar light (Intensity = 600 W·m^{-2}).

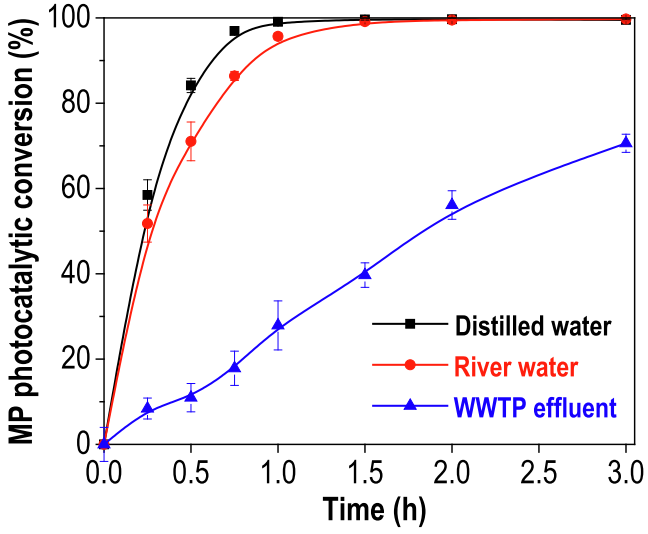

Fig. 5. Photocatalytic conversion of MP spiked in different water matrices under solar light ($[MP]_0 \approx$ 21.7 μM (after adsorption); UiO-66-NH_2 dose = 0.75 g·L^{-1}; Intensity = 600 W·m^{-2}).

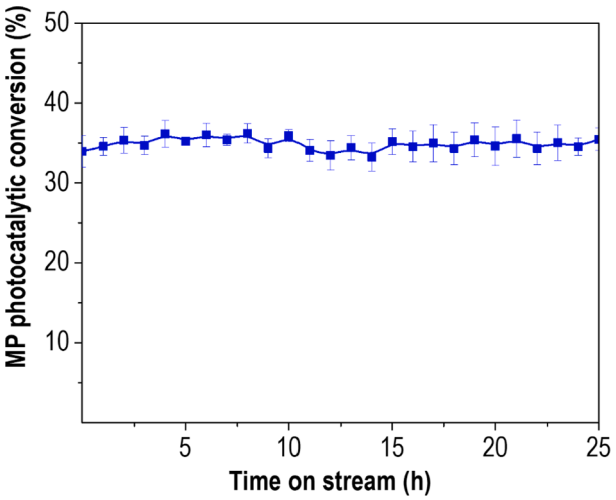

Fig. 6. Photocatalytic MP conversion upon time on stream (after reaching the steady state) in continuous experiment in slurry CSTR under solar light ($[MP]_0$ = 32.9 μM; [UiO-66-NH_2] = 0.75 g·L^{-1}; Flow-rate = 0.8 mL·min^{-1}; Intensity = 600 W·m^{-2}).

successive batch cycles. After each cycle, the resulting solid was recovered by filtration, rinsed with distilled water and dried at 60 °C overnight. Figure S7 displays the results obtained in terms of MP conversion. Only a slight reduction (around 4%) was observed after the fourth cycle with respect to the first one.

3.2.4. Proposed photocatalytic mechanism

To learn about the photocatalytic oxidation mechanism of MP using UiO-66-NH_2, a set of radical trapping experiments were carried out (Fig. 7). The good fitting of the apparent pseudo-first-order kinetic data is shown in Figure S8a and Table S4. The addition of KI (Fig. 7a) strongly influences the photocatalytic performance, decreasing k_{app} around 20-fold (Fig. 7b), indicating the determinant role of h^+ in the oxidation mechanism of MP. A remarkable conversion decrease was also found by the $O_2^{\bullet-}$ quenching effect of p-BQ. In contrast, the photocatalytic conversion of the target contaminant remained almost unaltered after adding 2-propanol and $AgNO_3$, suggesting a minor contribution of $HO^\bullet$ and e^-, respectively. The photocatalytic removal of parabens by means of the main contribution of $O_2^{\bullet-}$ and h^+ was also described in previous works reported by Guo et al. [59] and Xiao et al. [60], using different semiconductors than MOFs, as AgCl/Ag_3PO_4 and I-doped $Bi_4O_5Br_2$, respectively.

To better understand the photocatalyst performance, the Mott–Schottky electrochemical characterisation was used to determine the flat band potential, V_{FB}. As shown in Fig. 8a, a V_{FB} value of −0.82 V was registered from the interception with the potential axis at different frequencies. Then, a V_{CB} value of −0.78 V (*vs* NHE at pH 7) was obtained using Eq. (2). This V_{CB} was similar to the values already reported in the literature [30,61]. Besides, the V_{VB} was estimated to be 2.07 V (*vs* NHE at pH 7) following Eq. (3). The proposed bands structure and a tentative mechanism for the removal of MP using UiO-66-NH_2 under solar light are shown in Fig. 8b. It can be observed that the generation of $O_2^{\bullet-}$ by reduction of dissolved oxygen (-0.33 V *vs* NHE at pH 7) is energetically allowed, while the formation of $HO^\bullet$ is prevented. According to the results with scavengers displayed in Fig. 7, the aforementioned low contribution of $HO^\bullet$ can also be attributed to the leading role of h^+ as a direct oxidant of the MP, yielding to different byproducts that will be detailed in the next section.

Besides the proposed band structure, ESR spin-trap experiments were performed to detect the presence of the different species generated after UiO-66-NH_2 photoexcitation. Fig. 8c shows the ESR spectra of the TEMPO-h^+ adducts in the dark and under in situ UV radiation. TEMPO presents a stable triplet in the ESR spectrum that can be reduced by the holes, with a concomitant decrease in the ESR signal intensity [62,63]. The reduction of TEMPO-h^+ ESR strength upon irradiation supports the important contribution of holes in the oxidation mechanism. ESR experiments were also assessed with DMPO in different media to detect the presence of $O_2^{\bullet-}$ and $HO^\bullet$ radicals [64]. Fig. 8d shows no ESR signals in the dark with the catalyst dispersed in methanol. Under irradiation, the characteristic ESR signals of the DMPO-$O_2^{\bullet-}$ adduct can be seen [65], supporting the photogeneration of $O_2^{\bullet-}$ detected above. However, no ESR signals were detected during the ESR experiments performed in aqueous dispersion at different times. The absence of DMPO-$HO^\bullet$ adduct signals (Fig. 8e) reflects the non-formation of $HO^\bullet$ radicals, in agreement with the unfavourable formation of this radical proposed in the photocatalytic mechanism of MP removal using UiO-66-NH_2 (Fig. 8b).

3.2.5. Photocatalytic degradation pathway of MP

Fig. 9 displays a plausible photocatalytic degradation pathway of MP under solar light using UiO-66-NH_2, according to the byproducts identified by LC/ESI-MS analysis (results collected in Table S5). The molecular formula of the proposed byproducts was supported on low mass error (<±1 mDa) compared to the experimental mass and the registered number of rings and double bonds (RDB) in each molecule [66]. Up to three different oxidation routes were proposed. The first one consisted of the demethylation of the terminal C_8 methyl group and decarboxylation of C_1 from the parent compound, as previously reported [13], allowing

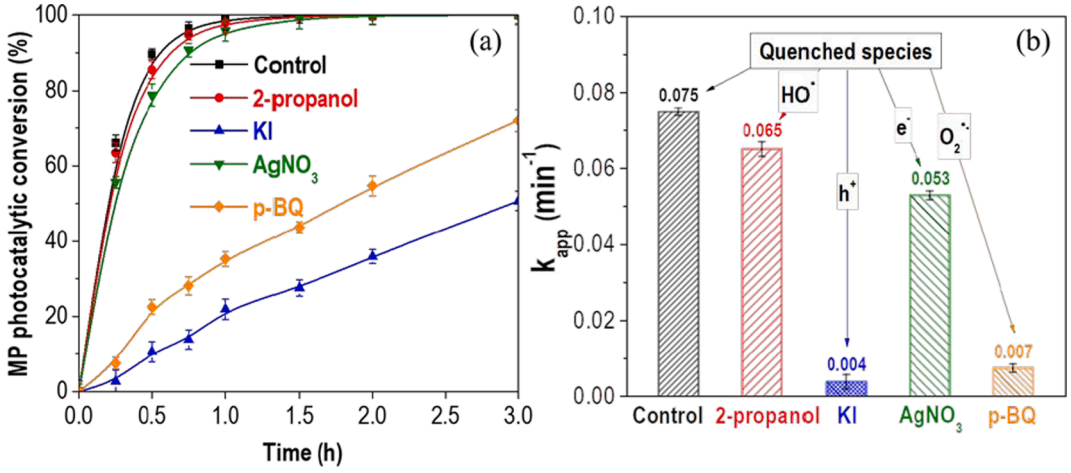

Fig. 7. (a) Photocatalytic conversion of MP in presence of different scavengers (1 mM), and (b) corresponding apparent pseudo-first-order rate (k_{app}, min^{-1}) under solar light ($[MP]_0 \approx$ 21.7 μM (after adsorption); UiO-66-NH_2 dose = 0.75 g·L^{-1}; Intensity = 600 W·m^{-2}).

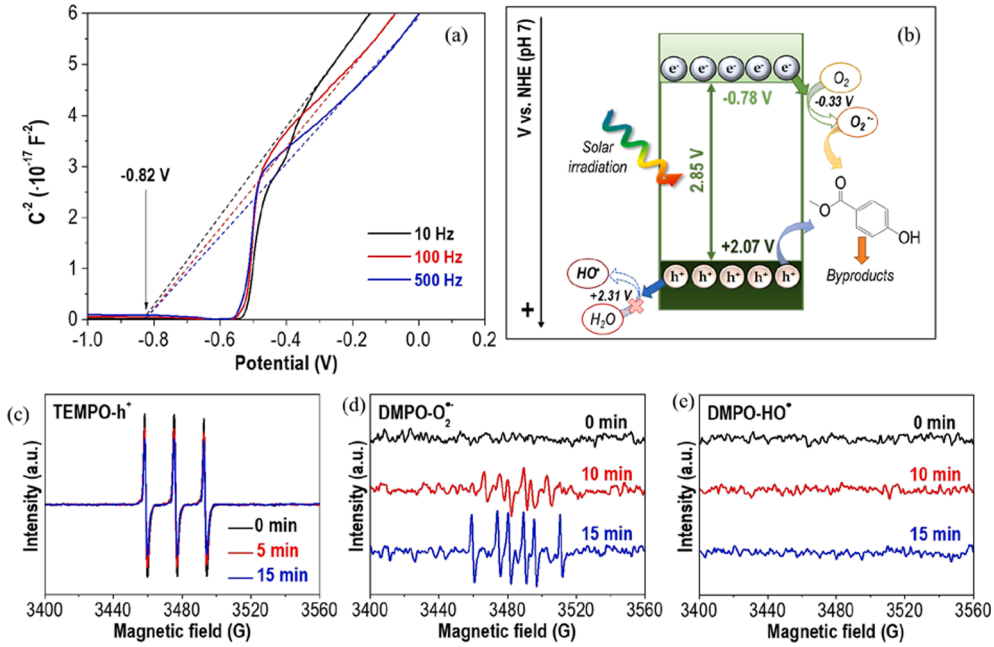

Fig. 8. (a) Mott-Schottky plot at three frequencies and (b) proposed photocatalytic mechanism of MP removal using UiO-66-NH_2. ESR spectra recorded in situ under UV radiation of (c) TEMPO-h^+, (d) DMPO-$O_2^{\bullet-}$ and (e) DMPO-$HO^{\bullet}$.

the formation of hydroquinone (MP-1*, not detected in this study) and p-benzoquinone (MP-1, *m/z* 109.0647) after further oxidation. These byproducts are commonly identified during the photocatalytic degradation of MP [67–70]. Subsequently, the ring opening followed by further oxidation would lead to the formation of the aliphatic byproducts MP-2 (*m/z* 163.1327) [13,71] and MP-3 (*m/z* 167.0553). The generation of MP-3 (2,3,4,5-tetrahydroxypentanoic acid), not previously reported as MP degradation byproduct, could be ascribed to a reiterative attack by oxidant species. Further oxidation would allow the generation of short-chain carboxylic acids, namely maleic, acrylic, acetic and formic acid (as identified by UHPLC).

The second oxidation route proposed in Fig. 9 was ascribed to the hydroxylation of MP, leading to the generation of MP-4 (*m/z* 169.0852). According to Tomita et al. [72], the addition of a hydroxyl group can be produced via: i) hydroxyl radical attack or even by ii) the attack of $O_2^{\bullet-}$ on the cationic radical form of the molecule obtained after direct oxidation by h^+. This second via would agree with the photocatalytic mechanism proposed in Fig. 8b. Moreover, it can be found in the literature [13,67–69,73] that hydroxylation can occur either in the aromatic ring or in the C_8 position. MP-4 can be further transformed into MP-2 and MP-3 intermediates through the opening of the aromatic ring, finally resulting in short-chain carboxylic acids. The third proposed route in Fig. 9 comprises an intramolecular coupling process involving the addition of alkyl moieties to the terminal C_8 methyl group, as reported in previous works [13,71]. In the current study, adding an isobutene moiety would allow the formation of the newly identified MP-5 (*m/z* 209.1172). A molecular coupling process could also be rationalised from MP-4 to generate MP-5.

The evolution of the identified intermediates was registered by UHPLC (Fig. 10a). It can be highlighted that MP-1 and MP-4 peaked after 60 and 30 min, respectively, and they were subsequently removed, whereas the formation of MP-3 appeared to be initiated after 45 min of photocatalytic treatment, in agreement with the degradation routes proposed in Fig. 9. The concentration profiles of the four identified short-chain carboxylic acids are depicted in Fig. 10b. It can be observed that formic acid rapidly reached its maximum concentration at 30 min, whereas acetic acid is continuously formed along with the experiment. Similar behaviour was registered for maleic and acrylic acids, but the concentration was two orders of magnitude lower.

Profiles depicted in Fig. 10 suggest that the synthesised MOF allows the complete conversion of parent MP and the progressive transformation of the identified byproducts into compounds of lower complexity.

3.2.6. *Degradation of different parabens*

The photocatalytic performance of UiO-66-NH_2 was also evaluated for removing other parabens, namely EP (ethylparaben) and PP (propylparaben). Fig. 11a shows the individual photocatalytic conversion of MP, EP and PP, conducted at a similar starting molar concentration (≈ 21.7 μM after adsorption) to ensure similar molecular interactions among the different parabens. It can be observed that the photocatalytic conversion decreased with the length of the alkyl side chain. This observation is at variance with what has been described in the literature with other photocatalysts whose reaction mechanism was controlled by $HO^{\bullet}$ [74]. It has been described that the apparent $k_{HO^{\bullet}}$ of parabens increased with the alkyl chain length [73]. Therefore, the lower activity observed with the increase in the length of the paraben alkyl side chain could be explained by the poor contribution of $HO^{\bullet}$ in the oxidation mechanism described in Section 3.2.4.

The conversion of the parabens was also studied in a mixture (Fig. 11b and S8b, and Table S6), reaching lower conversion values than in the individual tests. This difference could be due to competitive interactions with the catalyst surface, resulting in a parallel conversion of these parabens.

4. Conclusions

The photocatalytic removal of parabens using UiO-66-NH_2 under solar light was firstly reported in this work, showing outstanding performances compared to different photocatalysts previously reported.

Complete removal of MP was achieved in both distilled and river water samples, lowering when the contaminant was spiked in a WWTP effluent sample due to the higher concentrations of organic and inorganic species. The steady state of the photocatalytic performance in a continuous-flow regime was kept practically constant in a 25-h experiment, without structural and textural changes on the UiO-66-NH_2. That result opens a promising outlook for the potential future application of this photocatalyst.

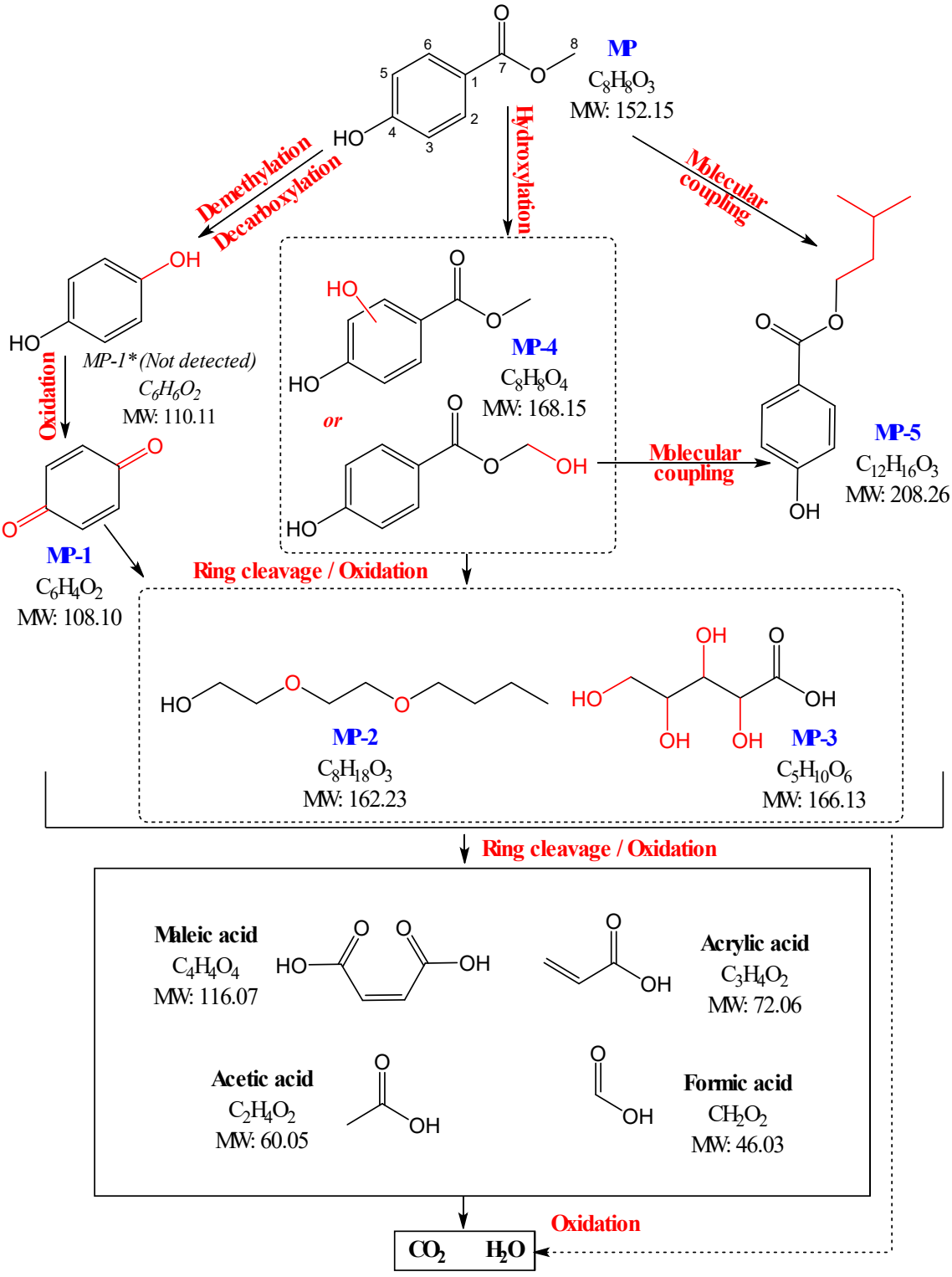

Fig. 9. Proposed photocatalytic degradation pathway of MP using UiO-66-NH_2.

The photocatalytic mechanism of MP degradation was found to occur mainly by h^+ and $O_2^{\bullet-}$. The interaction with those species led to the oxidation of MP and the identification of five intermediates (two of them not previously reported) and four short-chain carboxylic acids through three degradation routes involving demethylation followed by decarboxylation, hydroxylation, and molecular coupling. These findings will contribute to better understanding the consequences of paraben oxidation, addressing critical issues like the toxicity of the intermediates compared to the parent compounds.

The degradation difficulties when dealing with complex mixtures are evidenced when other parabens depicting high individual conversions, like EP and PP, become less prone to breakdown in the ternary mixture due to competitive reactions.

The current study demonstrates the stability of UiO-66-NH_2 in aqueous solution, making this system of potential interest for effective water treatment, especially with the increasing importance of water

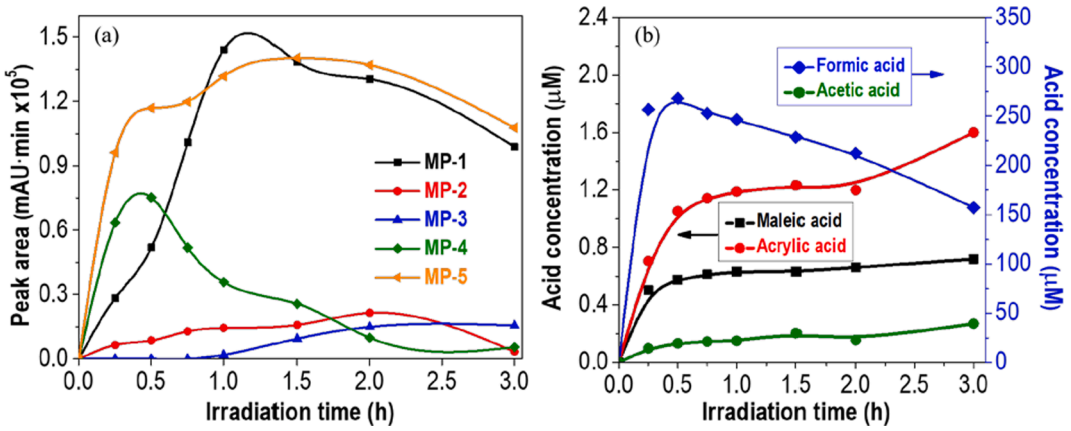

Fig. 10. Time-course evolution of the identified (a) byproducts and (b) short-chain carboxylic acids from the oxidation routes of MP using UiO-66-NH_2. ($[MP]_0$ = 329.0 μM; UiO-66-NH_2 dose = 0.75 g·L^{-1}; Intensity = 600 W·m^{-2}).

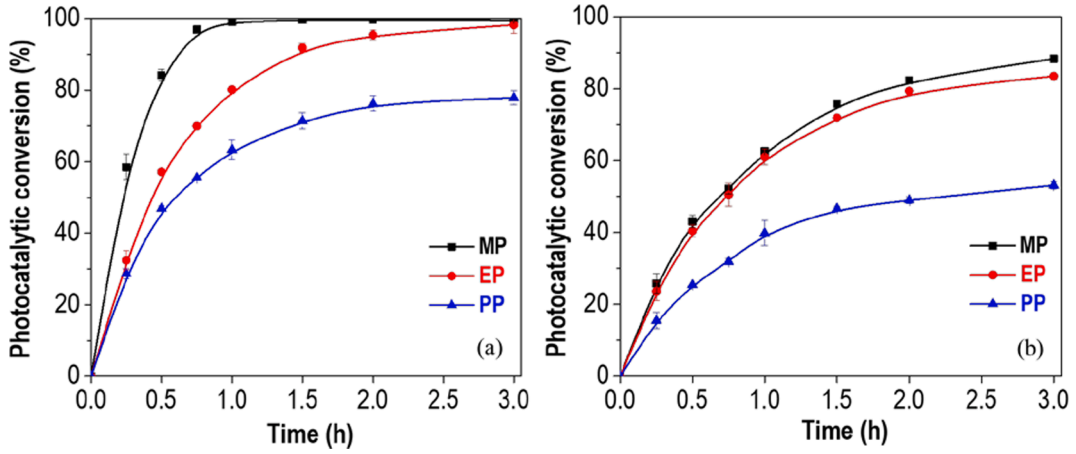

Fig. 11. Time-course photocatalytic conversion under solar light with UiO-66-NH_2 of (a) individual MP, EP and PP and (b) mixture of the three parabens ($[Paraben]_0$ ≈ 21.7 μM (after adsorption); UiO-66-NH_2 dose = 0.75 g·L^{-1}; Intensity = 600 W·m^{-2}).

reclamation. With a considerable part of the world population lacking access to clean water, MOFs stable in an aqueous environment can contribute to the next generation of materials to offer a breakthrough solution in water remediation.

Credit authorship contribution statement

All authors have contributed to the conceptualization, funding acquisition, data curation, formal analysis, investigation, methodology, validation, writing and editing roles.

Declaration of Competing Interest

The authors declare that they have no known competing financial interests or personal relationships that could have appeared to influence the work reported in this paper.

Acknowledgements

Authors acknowledge Spanish State Research Agency (PID2019-106186RBI00/AEI/10.13039/501100011033). M. Peñas-Garzón is indebted to Spanish MECD (FPU16/00576 grant) and MICIU (EST19/00068). M.J.S. thanks to Project POCI-01-0145-FEDER-030674 (MicroPhotOGen, PTDC/NAN-MAT/30674/2017) funded by ERDF through COMPETE2020 - Programa Operacional Competitividade e Internacionalização (POCI) – and by national funds through FCT - Fundação para a Ciência e a Tecnologia. We would like to thank the scientific collaboration financially supported by: Base-UIDB/50020/2020 and Programmatic-UIDP/50020/2020 Funding of Associate Laboratory LSRE-LCM - funded by national funds through FCT/MCTES (PIDDAC). Authors thank the Research Support Services of the Universidad Autónoma de Madrid (SIdI), University of Extremadura (SAIUEx), University of Málaga (SCAI) and Universidad Complutense of Madrid (CAI).

Appendix A. Supplementary material

Supplementary data to this article can be found online at https://doi.org/10.1016/j.seppur.2022.120467.

References

[1] N. Matwiejczuk, A. Galicka, M.M. Brzóska, Review of the safety of application of cosmetic products containing parabens, J. Appl. Toxicol. 40 (1) (2020) 176–210, https://doi.org/10.1002/jat.3917.

[2] N.B. Bolujoko, E.I. Unuabonah, M.O. Alfred, A. Ogunlaja, O.O. Ogunlaja, M. O. Omorogie, O.D. Olukanni, Toxicity and removal of parabens from water: A critical review, Sci. Total Environ. 792 (2021) 148092, https://doi.org/10.1016/j.scitotenv.2021.148092.

[3] Commission Regulation (EU) No 1004/2014 of 18 September 2014 amending Annex V to Regulation (EC) No 1223/2009 of the European Parliament and of the Council on cosmetic products, Off. J. Eur. Union. (2014). https://eur-lex.europa.eu/legal-content/EN/TXT/?uri=CELEX%3A32014R1004.

[4] A.J. Spanier, T. Fausnight, T.F. Camacho, J.M. Braun, The associations of triclosan and paraben exposure with allergen sensitization and wheeze in children, Allergy Asthma Proc. 35 (6) (2014) 475–481, https://doi.org/10.2500/aap.2014.35.3803.

[5] E.P. Hines, P. Mendola, O.S. von Ehrenstein, X. Ye, A.M. Calafat, S.E. Fenton, Concentrations of environmental phenols and parabens in milk, urine and serum of lactating North Carolina women, Reprod. Toxicol. 54 (2015) 120–128, https://doi.org/10.1016/j.reprotox.2014.11.006.

[6] C.M. Glover, Y. Liu, J. Liu, Assessing the risk from trace organic contaminants released via greywater irrigation to the aquatic environment, Water Res. 205 (2021) 117664, https://doi.org/10.1016/j.watres.2021.117664.

[7] W. Wang, K. Kannan, Fate of Parabens and Their Metabolites in Two Wastewater Treatment Plants in New York State, United States, Environ. Sci. Technol. 50 (3) (2016) 1174–1181, https://doi.org/10.1021/acs.est.5b05516.

[8] Z. Frontistis, M. Antonopoulou, A. Petala, D. Venieri, I. Konstantinou, D. I. Kondarides, D. Mantzavinos, Photodegradation of ethyl paraben using simulated solar radiation and Ag_3PO_4 photocatalyst, J. Hazard. Mater. 323 (2017) 478–488, https://doi.org/10.1016/j.jhazmat.2016.04.017.

[9] V. Acevedo-García, E. Rosales, A. Puga, M. Pazos, M.A. Sanromán, Synthesis and use of efficient adsorbents under the principles of circular economy: Waste valorisation and electroadvanced oxidation process regeneration, Sep. Purif. Technol. 242 (2020) 116796, https://doi.org/10.1016/j.seppur.2020.116796.

[10] J. Lu, H. Li, Y. Tu, Z. Yang, Biodegradation of four selected parabens with aerobic activated sludge and their transesterification product, Ecotoxicol. Environ. Saf. 156 (2018) 48–55, https://doi.org/10.1016/j.ecoenv.2018.02.078.

[11] J.F. Gomes, A. Lopes, M. Gmurek, R.M. Quinta-Ferreira, R.C. Martins, Study of the influence of the matrix characteristics over the photocatalytic ozonation of parabens using Ag-TiO_2, Sci. Total Environ. 646 (2019) 1468–1477, https://doi.org/10.1016/j.scitotenv.2018.07.430.

[12] N. Vela, M. Calín, M.J. Yáñez-Gascón, I. Garrido, G. Pérez-Lucas, J. Fenoll, S. Navarro, Solar reclamation of wastewater effluent polluted with bisphenols, phthalates and parabens by photocatalytic treatment with $TiO_2/Na_2S_2O_8$ at pilot plant scale, Chemosphere. 212 (2018) 95–104, https://doi.org/10.1016/j.chemosphere.2018.08.069.

[13] T. Velegraki, E. Hapeshi, D. Fatta-Kassinos, I. Poulios, Solar-induced heterogeneous photocatalytic degradation of methyl-paraben, Appl. Catal. B Environ. 178 (2015) 2–11, https://doi.org/10.1016/j.apcatb.2014.11.022.

[14] S. Kotzamanidi, Z. Frontistis, V. Binas, G. Kiriakidis, D. Mantzavinos, Solar photocatalytic degradation of propyl paraben in Al-doped TiO_2 suspensions, Catal. Today. 313 (2018) 148–154, https://doi.org/10.1016/j.cattod.2017.12.006.

[15] V.-H. Nguyen, L.-A. Phan Thi, P.S. Chandana, H.-T. Do, T.-H. Pham, T. Lee, T. D. Nguyen, C. Le Phuoc, P.T. Huong, The degradation of paraben preservatives: Recent progress and sustainable approaches toward photocatalysis, Chemosphere 276 (2021) 130163, https://doi.org/10.1016/j.chemosphere.2021.130163.

[16] H. Zúñiga-Benítez, G.A. Peñuela, Methylparaben removal using heterogeneous photocatalysis: effect of operational parameters and mineralization/biodegradability studies, Environ. Sci. Pollut. Res. 24 (7) (2017) 6022–6030, https://doi.org/10.1007/s11356-016-6468-9.

[17] R.A. Fernandes, M.J. Sampaio, G. Dražić, J.L. Faria, C.G. Silva, Efficient removal of parabens from real water matrices by a metal-free carbon nitride photocatalyst, Sci. Total Environ. 716 (2020) 135346, https://doi.org/10.1016/j.scitotenv.2019.135346.

[18] X. Xiao, S. Tu, M. Lu, H. Zhong, C. Zheng, X. Zuo, J. Nan, Discussion on the reaction mechanism of the photocatalytic degradation of organic contaminants from a viewpoint of semiconductor photo-induced electrocatalysis, Appl. Catal. B Environ. 198 (2016) 124–132, https://doi.org/10.1016/j.apcatb.2016.05.042.

[19] E. Sharmin, F. Zafar, in: Metal-Organic Frameworks, InTech, 2016, https://doi.org/10.5772/64797.

[20] J. Bedia, V. Muelas-Ramos, M. Peñas-Garzón, A. Gómez-Avilés, J. Rodríguez, C. Belver, A Review on the Synthesis and Characterization of Metal Organic Frameworks for Photocatalytic Water Purification, Catalysts. 9 (1) (2019) 52, https://doi.org/10.3390/catal9010052.

[21] J. Gascon, A. Corma, F. Kapteijn, F.X. Llabrés I Xamena, Metal organic framework catalysis: Quo vadis?, ACS Catal. 4 (2014) 361–378. https://doi.org/10.1021/cs400959k.

[22] J. Bedia, V. Muelas-Ramos, M. Peñas-Garzón, A. Gómez-Avilés, J.J. Rodriguez, C. Belver, Metal–organic frameworks for water purification, in: B. Bonelli, F. S. Freyria, I. Rossetti, R. Sethi (Eds.), Nanomater, Elsevier, Detect. Remov. Wastewater Pollut., 2020, pp. 241–283.

[23] A. Gómez-Avilés, M. Peñas-Garzón, J. Bedia, D.D. Dionysiou, J.J. Rodríguez, C. Belver, Mixed Ti-Zr metal-organic-frameworks for the photodegradation of acetaminophen under solar irradiation, Appl. Catal. B Environ. 253 (2019) 253–262, https://doi.org/10.1016/j.apcatb.2019.04.040.

[24] V. Muelas-Ramos, M.J. Sampaio, C.G. Silva, J. Bedia, J.J. Rodriguez, J.L. Faria, C. Belver, Degradation of diclofenac in water under LED irradiation using combined g-C_3N_4/NH_2-MIL-125 photocatalysts, J. Hazard. Mater. 416 (2021) 126199, https://doi.org/10.1016/j.jhazmat.2021.126199.

[25] L. Xie, Z. Yang, W. Xiong, Y. Zhou, J. Cao, Y. Peng, X. Li, C. Zhou, R. Xu, Y. Zhang, Construction of MIL-53(Fe) metal-organic framework modified by silver phosphate nanoparticles as a novel Z-scheme photocatalyst: Visible-light photocatalytic performance and mechanism investigation, Appl. Surf. Sci. 465 (2019) 103–115, https://doi.org/10.1016/j.apsusc.2018.09.144.

[26] D. Tilgner, M. Friedrich, A. Verch, N. deJonge, R. Kempe, A Metal-Organic Framework Supported Nonprecious Metal Photocatalyst for Visible-Light-Driven Wastewater Treatment, ChemPhotoChem. 2 (4) (2018) 349–352, https://doi.org/10.1002/cptc.201700222.

[27] X.D. Du, X.H. Yi, P. Wang, W. Zheng, J. Deng, C.C. Wang, Robust photocatalytic reduction of Cr(VI) on UiO-66-NH_2(Zr/Hf) metal-organic framework membrane under sunlight irradiation, Chem. Eng. J. 356 (2019) 393–399, https://doi.org/10.1016/j.cej.2018.09.084.

[28] X. Mu, J. Jiang, F. Chao, Y. Lou, J. Chen, Ligand modification of UiO-66 with an unusual visible light photocatalytic behavior for RhB degradation, Dalt. Trans. 47 (6) (2018) 1895–1902.

[29] C. Du, Z. Zhang, G. Yu, H. Wu, H. Chen, L.u. Zhou, Y. Zhang, Y. Su, S. Tan, L. u. Yang, J. Song, S. Wang, A review of metal organic framework (MOFs)-based materials for antibiotics removal via adsorption and photocatalysis, Chemosphere. 272 (2021) 129501, https://doi.org/10.1016/j.chemosphere.2020.129501.

[30] Y.L. Wang, S. Zhang, Y.F. Zhao, J. Bedia, J.J. Rodriguez, C. Belver, UiO-66-based metal organic frameworks for the photodegradation of acetaminophen under simulated solar irradiation, J. Environ. Chem. Eng. 9 (5) (2021) 106087, https://doi.org/10.1016/j.jece:2021.106087.

[31] Q. Du, P.u. Wu, Y. Sun, J. Zhang, H. He, Selective photodegradation of tetracycline by molecularly imprinted ZnO@NH_2-UiO-66 composites, Chem. Eng. J. 390 (2020) 124614, https://doi.org/10.1016/j.cej.2020.124614.

[32] S. Zhang, Y. Wang, Z. Cao, J. Xu, J. Hu, Y. Huang, C. Cui, H. Liu, H. Wang, Simultaneous enhancements of light-harvesting and charge transfer in UiO-67/CdS/rGO composites toward ofloxacin photo-degradation, Chem. Eng. J. 381 (2020) 122771, https://doi.org/10.1016/j.cej.2019.122771.

[33] A. Nandy, A.C. Forse, V.J. Witherspoon, J.A. Reimer, NMR Spectroscopy Reveals Adsorbate Binding Sites in the Metal-Organic Framework UiO-66(Zr), J. Phys. Chem. C. 122 (15) (2018) 8295–8305, https://doi.org/10.1021/acs.jpcc.7b12628.

[34] S. Brunauer, P.H. Emmett, E. Teller, Adsorption of Gases in Multimolecular Layers, J. Am. Chem. Soc. 60 (1938) 309–319. https://doi.org/10.1021/ja01269a023.

[35] B.C. Lippens, de B. J.H., Studies on pore systems in catalysts: V. The t method, J. Catal. 4 (1965) 319–323. https://doi.org/10.1016/0021-9517(65)90307-6.

[36] J. Tauc, Absorption edge and internal electric fields in amorphous semiconductors, Mater. Res. Bull. 5 (8) (1970) 721–729, https://doi.org/10.1016/0025-5408(70)90112-1.

[37] G. Newcombe, R. Hayes, M. Drikas, Granular activated carbon: Importance of surface properties in the adsorption of naturally occurring organics, Colloids Surf. A Physicochem. Eng. Asp. 78 (1993) 65–71, https://doi.org/10.1016/0927-7757(93)80311-2.

[38] C. Baumanis, D.W. Bahnemann, TiO_2 thin film electrodes: Correlation between photocatalytic activity and electrochemical properties, J. Phys. Chem. C. 112 (48) (2008) 19097–19101, https://doi.org/10.1021/jp807655a.

[39] T. Giannakopoulou, I. Papailias, N. Todorova, N. Boukos, Y. Liu, J. Yu, C. Trapalis, Tailoring the energy band gap and edges' potentials of g-C_3N_4/TiO_2 composite photocatalysts for NO_x removal, Chem. Eng. J. 310 (2017) 571–580, https://doi.org/10.1016/J.CEJ.2015.12.102.

[40] R.P. Cavalcante, R.F. Dantas, B. Bayarri, O. González, J. Giménez, S. Esplugas, A. Machulek, Photocatalytic mechanism of metoprolol oxidation by photocatalysts TiO_2 and TiO_2 doped with 5% B: Primary active species and intermediates, Appl. Catal. B Environ. 194 (2016) 111–122, https://doi.org/10.1016/j.apcatb.2016.04.054.

[41] A.P.H. Association, Standard methods for the examination of water and wastewater, 23 ed, APHA, Washington, 2017.

[42] Z. Yang, X. Tong, J. Feng, S. He, M. Fu, X. Niu, T. Zhang, H. Liang, A. Ding, X. Feng, Flower-like BiOBr/UiO-66-NH_2 nanosphere with improved photocatalytic property for norfloxacin removal, Chemosphere. 220 (2019) 98–106, https://doi.org/10.1016/j.chemosphere.2018.12.086.

[43] J.F. Moulder, W.F. Stickle, P.E. Sobol, K.D. Bomben, Handbook of X-Ray Photoelectron Spectroscopy, Eden Prairie, MN, Perkin-Elmer, 1992, p. 2002.

[44] Q. Liang, S. Cui, C. Liu, S. Xu, C. Yao, Z. Li, Construction of CdS@UIO-66-NH_2 core-shell nanorods for enhanced photocatalytic activity with excellent photostability, J. Colloid Interface Sci. 524 (2018) 379–387, https://doi.org/10.1016/j.jcis.2018.03.114.

[45] X. Fang, S. Wu, Y. Wu, W.u. Yang, Y. Li, J. He, P. Hong, M. Nie, C. Xie, Z. Wu, K. Zhang, L. Kong, J. Liu, High-efficiency adsorption of norfloxacin using octahedral UIO-66-NH_2 nanomaterials: Dynamics, thermodynamics, and mechanisms, Appl. Surf. Sci. 518 (2020) 146226, https://doi.org/10.1016/j.apsusc.2020.146226.

[46] Q. Chen, Q. He, M. Lv, Y. Xu, H. Yang, X. Liu, F. Wei, Selective adsorption of cationic dyes by UiO-66-NH_2, Appl. Surf. Sci. 327 (2015) 77–85, https://doi.org/10.1016/j.apsusc.2014.11.103.

[47] J. Ren, S. Lv, S. Wang, M. Bao, X. Zhang, Y. Gao, Y. Liu, Z. Zhang, L. Zeng, J. Ke, Construction of efficient g-C_3N_4/NH_2-UiO-66 (Zr) heterojunction photocatalysts for wastewater purification, Sep. Purif. Technol. 274 (2021) 118973, https://doi.org/10.1016/j.seppur.2021.118973.

[48] Y. Cao, H. Zhang, F. Song, T. Huang, J. Ji, Q. Zhong, W. Chu, Q. Xu, UiO-66-NH_2/GO composite: Synthesis, characterization and CO_2 adsorption performance, Materials (Basel). 11 (2018) 589, https://doi.org/10.3390/ma11040589.

[49] K. Chakarova, I. Strauss, M. Mihaylov, N. Drenchev, K. Hadjiivanov, Evolution of acid and basic sites in UiO-66 and UiO-66-NH_2 metal-organic frameworks: FTIR study by probe molecules, Microporous Mesoporous Mater. 281 (2019) 110–122, https://doi.org/10.1016/j.micromeso.2019.03.006.

[50] J.H. Cavka, S. Jakobsen, U. Olsbye, N. Guillou, C. Lamberti, S. Bordiga, K. P. Lillerud, A new zirconium inorganic building brick forming metal organic frameworks with exceptional stability, J. Am. Chem. Soc. 130 (42) (2008) 13850–13851, https://doi.org/10.1021/ja8057953.

[51] S.N. Tambat, P.K. Sane, S. Suresh, N. Varadan O., A.B. Pandit, S.M. Sontakke, Hydrothermal synthesis of NH_2-UiO-66 and its application for adsorptive removal

of dye, Adv. Powder Technol. 29 (2018) 2626–2632. https://doi.org/10.1016/j.apt.2018.07.010.
[52] S. Jamshidifard, S. Koushkbaghi, S. Hosseini, S. Rezaei, A. Karamipour, A. Jafari rad, M. Irani, Incorporation of UiO-66-NH_2 MOF into the PAN/chitosan nanofibers for adsorption and membrane filtration of Pb(II), Cd(II) and Cr(VI) ions from aqueous solutions, J. Hazard. Mater. 368 (2019) 10–20, https://doi.org/10.1016/j.jhazmat.2019.01.024.
[53] J. Long, S. Wang, Z. Ding, S. Wang, Y. Zhou, L. Huang, X. Wanga, Amine-functionalized zirconium metal–organic framework as efficient visible-light photocatalyst for aerobic organic transformations, Chem. Commun. 48 (2012) 11656–11658, https://doi.org/10.1039/c2cc34620f.
[54] C. Wang, H. Lin, Z. Xu, H. Cheng, C. Zhang, One-step hydrothermal synthesis of flowerlike MoS_2/CdS heterostructures for enhanced visible-light photocatalytic activities, RSC Adv. 5 (20) (2015) 15621–15626, https://doi.org/10.1039/C4RA15632C.
[55] A.R. Lado Ribeiro, N.F.F. Moreira, G. Li Puma, A.M.T. Silva, Impact of water matrix on the removal of micropollutants by advanced oxidation technologies, Chem. Eng. J. 363 (2019) 155–173, https://doi.org/10.1016/j.cej.2019.01.080.
[56] Y. Wu, F. Wang, X. Jin, X. Zheng, Y. Wang, D. Wei, Q. Zhang, Y. Feng, Z. Xie, P. Chen, H. Liu, G. Liu, Highly active metal-free carbon dots/g-C_3N_4 hollow porous nanospheres for solar-light-driven PPCPs remediation: Mechanism insights, kinetics and effects of natural water matrices, Water Res. 172 (2020) 115492, https://doi.org/10.1016/j.watres.2020.115492.
[57] C.S. Uyguner-Demirel, N.C. Birben, M. Bekbolet, Elucidation of background organic matter matrix effect on photocatalytic treatment of contaminants using TiO_2: A review, Catal. Today. 284 (2017) 202–214, https://doi.org/10.1016/j.cattod.2016.12.030.
[58] N. Rioja, S. Zorita, F.J. Peñas, Effect of water matrix on photocatalytic degradation and general kinetic modeling, Appl. Catal. B Environ. 180 (2016) 330–335, https://doi.org/10.1016/j.apcatb.2015.06.038.
[59] J. Guo, H. Shi, X. Huang, H. Shi, Z. An, AgCl/Ag_3PO_4: A stable Ag-Based nanocomposite photocatalyst with enhanced photocatalytic activity for the degradation of parabens, J. Colloid Interface Sci. 515 (2018) 10–17, https://doi.org/10.1016/j.jcis.2018.01.015.
[60] X. Xiao, M. Lu, J. Nan, X. Zuo, W. Zhang, S. Liu, S. Wang, Rapid microwave synthesis of I-doped Bi_4O_5Br 2 with significantly enhanced visible-light photocatalysis for degradation of multiple parabens, Appl. Catal. B Environ. 218 (2017) 398–408, https://doi.org/10.1016/j.apcatb.2017.06.074.
[61] X. Wang, X. Zhao, D. Zhang, G. Li, H. Li, Microwave irradiation induced UIO-66-NH_2 anchored on graphene with high activity for photocatalytic reduction of CO_2, Appl. Catal. B Environ. 228 (2018) 47–53, https://doi.org/10.1016/J.APCATB.2018.01.066.
[62] W. He, J. Cai, X. Jiang, J.-J. Yin, Q. Meng, Generation of reactive oxygen species and charge carriers in plasmonic photocatalytic Au@TiO_2 nanostructures with enhanced activity, Phys. Chem. Chem. Phys. 20 (23) (2018) 16117–16125.
[63] Y. Wu, X. Li, Q.i. Yang, D. Wang, F. Yao, J. Cao, Z. Chen, X. Huang, Y. Yang, X. Li, Mxene-modulated dual-heterojunction generation on a metal-organic framework (MOF) via surface constitution reconstruction for enhanced photocatalytic activity, Chem. Eng. J. 390 (2020) 124519, https://doi.org/10.1016/j.cej.2020.124519.
[64] Z. Wang, W. Ma, C. Chen, H. Ji, J. Zhao, Probing paramagnetic species in titania-based heterogeneous photocatalysis by electron spin resonance (ESR) spectroscopy-A mini review, Chem. Eng. J. 170 (2-3) (2011) 353–362, https://doi.org/10.1016/j.cej.2010.12.002.
[65] B. Wang, C. Li, H. Cui, J. Zhang, J. Zhai, Q. Li, Fabrication and enhanced visible-light photocatalytic activity of Pt-deposited TiO_2 hollow nanospheres, Chem. Eng. J. 223 (2013) 592–603, https://doi.org/10.1016/j.cej.2013.03.052.
[66] M. Peñas-Garzón, W.H.M. Abdelraheem, C. Belver, J.J. Rodriguez, J. Bedia, D. D. Dionysiou, TiO_2-carbon microspheres as photocatalysts for effective remediation of pharmaceuticals under simulated solar light, Sep. Purif. Technol. 275 (2021) 119169, https://doi.org/10.1016/j.seppur.2021.119169.
[67] J. Gomes, J. Lincho, E. Domingues, M. Gmurek, P. Mazierski, A. Zaleska-Medynska, T. Klimczuk, R.M. Quinta-Ferreira, R.C. Martins, TiO_2 nanotube arrays-based reactor for photocatalytic oxidation of parabens mixtures in ultrapure water: Effects of photocatalyst properties, operational parameters and light source, Sci. Total Environ. 689 (2019) 79–89, https://doi.org/10.1016/j.scitotenv.2019.06.410.
[68] X. Zhang, X. Wang, J. Meng, Y. Liu, M. Ren, Y. Guo, Y. Yang, Robust Z-scheme g-C_3N_4/WO_3 heterojunction photocatalysts with morphology control of WO_3 for efficient degradation of phenolic pollutants, Sep. Purif. Technol. 255 (2021) 117693, https://doi.org/10.1016/j.seppur.2020.117693.
[69] Y. Liu, P. Xia, L. Li, X. Wang, J. Meng, Y. Yang, Y. Guo, In-situ route for the graphitized carbon/TiO_2 composite photocatalysts with enhanced removal efficiency to emerging phenolic pollutants, Chinese, J. Catal. 41 (9) (2020) 1378–1392, https://doi.org/10.1016/S1872-2067(20)63565-3.
[70] J.F. Gomes, I. Leal, K. Bednarczyk, M. Gmurek, M. Stelmachowski, M. Diak, M. Emília Quinta-Ferreira, R. Costa, R.M. Quinta-Ferreira, R.C. Martins, Photocatalytic ozonation using doped TiO_2 catalysts for the removal of parabens in water, Sci. Total Environ. 609 (2017) 329–340, https://doi.org/10.1016/j.scitotenv.2017.07.180.
[71] Y. Lin, C. Ferronato, N. Deng, F. Wu, J.-M. Chovelon, Photocatalytic degradation of methylparaben by TiO_2: Multivariable experimental design and mechanism, Appl. Catal. B Environ. 88 (1-2) (2009) 32–41, https://doi.org/10.1016/j.apcatb.2008.09.026.
[72] O. Tomita, B. Ohtani, R. Abe, Highly selective phenol production from benzene on a platinum-loaded tungsten oxide photocatalyst with water and molecular oxygen: Selective oxidation of water by holes for generating hydroxyl radical as the predominant source of the hydroxyl group, Catal. Sci. Technol. 4 (11) (2014) 3850–3860.
[73] K.S. Tay, N.A. Rahman, M.R.B. Abas, Ozonation of parabens in aqueous solution: Kinetics and mechanism of degradation, Chemosphere. 81 (11) (2010) 1446–1453, https://doi.org/10.1016/j.chemosphere.2010.09.004.
[74] S. Klementova, D. Kahoun, L. Doubkova, K. Frejlachova, M. Dusakova, M. Zlamal, Catalytic photodegradation of pharmaceuticals-homogeneous and heterogeneous photocatalysis, Photochem. Photobiol. Sci. 16 (1) (2017) 67–71.